

# Effects of Local and Nonlocal Substructure Spin on Localization in Tantalum Top-Hat Specimen

D. Luscher, C. Bronkhorst, D. McDowell

*Effects of local and nonlocal substructure spin on the localization behavior of tantalum top-hat specimens subjected to high-rate compression are investigated. The orientation of a quadratic yield surface within the space of the intermediate configuration second Piola Kirchhoff stress is defined by a triad of substructure unit director vectors. Local evolution kinetics for the substructure directors are based on a plastic constitutive spin proportional to the non-coaxiality between stress and plastic rate of deformation within the spinless intermediate configuration. An extension of the local plastic constitutive spin to reflect nonlocal kinetics is made by attenuating or amplifying the spin rate depending on the misorientation of the substructure directors at a material point with those at adjacent material points within some neighborhood. Increased local spin rates tend to accentuate localization of plastic deformation and acts as a constitutive softening mechanism. On the other hand, the constraint imposed by nonlocal evolution of substructure orientation affects the plastic deformation field by reducing the propensity for flow, thus delaying localization and increasing the spatial coherence of the director vector field.*

## 1 Introduction

During high strain-rate deformation of polycrystalline metals, locally concentrated deformation is typically a precursor to strong localization. The latter can be appreciated from differing perspectives; physically, the effective material stiffness degrades such that additional deformation within a region is most easily accommodated within an ever collapsing localized region, mathematically, the boundary value problem has changed in character, e.g. a loss of hyperbolicity, which is manifest in a non-positive definite acoustic tensor. Such conditions often lead to the formation of localization (or shear) bands in the material. Localization is triggered by apparent constitutive softening, i.e., a decrease in the tangent stiffness of the material's stress-strain response. Softening mechanisms in polycrystalline metals include heat generation from inelastic dissipation, accumulation of damage, and reorientation of the yield surface into a configuration more favorable for inelastic flow.

The initiation and growth of such shear bands has significant influence on the development of macroscale fracture and potential for subsequent fragmentation. In order for macroscale models to be predictive in cases of fragmentation, the constitutive approach must adequately capture the details of deformation localization, especially aspects that attenuate or accentuate the formation of shear bands.

A classic laboratory specimen for investigating deformation localization is the so-called top-hat specimen (Nemat-Nasser et al., 1994; Bronkhorst et al., 2006). As illustrated in Figure 1, the specimen consists of an upper hat region and a lower brim region separated by a shear zone. The shear zone is so named because the configuration causes localization and shear bands (if they form) to occur in this predetermined location. Bronkhorst et al. (2006, 2007) conducted numerical and experimental investigations into the formation of shear bands in stainless steel top-hat specimen and lack thereof for tantalum specimen. In that work, top-hat specimens were loaded under compression at a high rate in a split Hopkinson pressure bar (SHPB) apparatus. Bronkhorst et al. (2006) note that while shear band instabilities did not form for tantalum specimen, localized shear deformation was accommodated by extensive grain rotation and elongation. This alludes to reorientation of the lattice, an inference generally supported by electron backscatter diffraction (EBSD) data collected from the shear zone region prior to and after the experiments as shown in Figure 2.

From these observations, a natural question arises as to the influence of substructure reorientation on the localization behavior. Does such reorientation merely accompany the deformation process whose localization characteristics are dominated by thermal softening and heat generation, or does such reorientation enhance the localization process in its own right? This is one of two central questions addressed by the present paper.

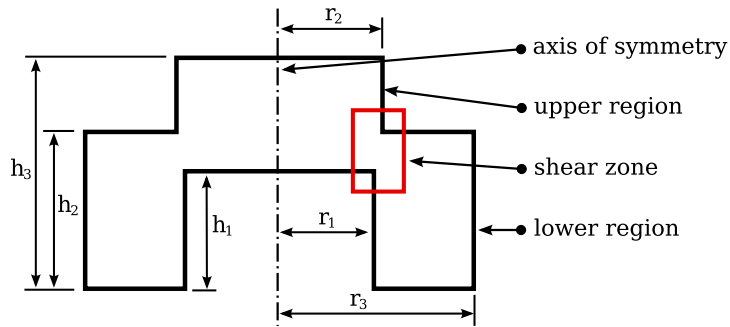


Figure 1: Top-hat specimen geometry and key dimensions

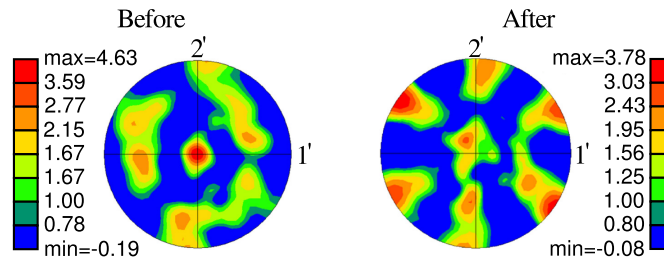


Figure 2: Before and after pole figures

A review of relevant literature reinforces the idea that reorientation of preferred directions in the substructure of the material has consequence to the localization behavior (Kuroda, 1996; Tvergaard and van der Giessen, 1991; Zbib and Aifantis, 1988a,b; Zbib, 1993; Dafalias, 1998, 2000; Lee et al., 1995). Amongst the expansive work of Dafalias establishing the importance of constitutive aspects of plastic spin, substructure orientation evolution was asserted to be an important aspect of localization (Dafalias, 1998). Zbib and Aifantis (1988a,b) and later Zbib (1993) defined the plastic constitutive spin (although this terminology was not introduced at that time) using the non-coaxiality between the Cauchy stress and plastic rate of deformation tensor. Lee et al. (1995) used a hypoelastic stress-update scheme whose objective stress-rate was based on plastic spin associated with non-coaxiality of the stress and plastic rate of deformation to show that reorientation of orthotropic material axes can hasten or delay strain localization. Similarly, Tvergaard and van der Giessen (1991) assessed the influence of different stress-rates, some of which employed plastic spin, on localization behavior. Kuroda (1996) cast the problem in the current configuration with a hypoelastic update scheme showing that *increasing* plastic spin *delayed* or prevented localization in simulations of plane strain tension.

Presuming, in this introduction, that reorientation of underlying material substructure has important consequence to localization behavior, another question arises. Are nonlocal kinetics for substructure evolution important to the localization behavior? Clearly, it is the collective reorientation of the crystal lattice associated with neighborhoods of grains that leads to evolution of polycrystal anisotropy. Bunge and Nielsen (1997) show that after strong texture forms, grains with close orientation remain grouped together during subsequent deformation. This suggests nonlocal evolution kinetics may be appropriate. A supporting physical argument is that there should be some energetic consequence penalizing sharp contrast in substructure orientation, i.e., substructure at adjacent material points should not spin independently. This question is the second central focus of the present paper. Having introduced the two underlying questions, i.e.,

- Does substructure reorientation enhance the localization process?
- Are nonlocal kinetics for substructure evolution important to the localization behavior?

The remainder of this paper is organized as follows in order to address these questions in the context of high rate deformation of tantalum top-hat specimens. Section 2 presents the constitutive framework employing finite deformation strain measures in a hyperelastic setting. Details of the numerical implementation and simulations are given in Section 3 and a discussion of the generated results is provided in Section 4. A summary of the paper with conclusions is provided in Section 5.

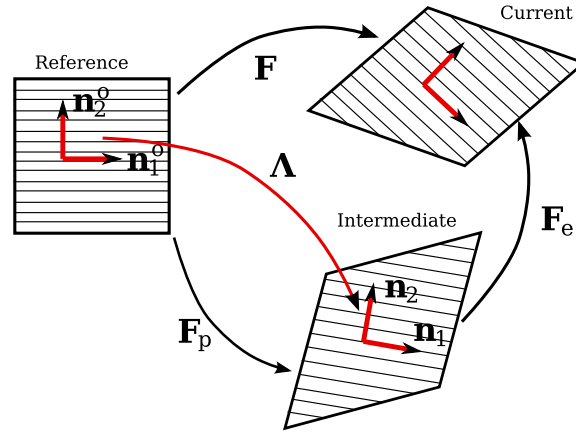


Figure 3: Configurations corresponding to multiplicative decomposition with substructure orientation.

## 2 Anisotropic Constitutive Framework with Substructure Spin

In particular, we address constitutive response that is described with an initial orthotropic symmetry although the framework is readily extended to other cases of material symmetry or induced anisotropy. In the orthotropic case there exists a set of orthogonal unit vectors defining the orientation of material symmetry, i.e.,  $\mathbf{n}_1, \mathbf{n}_2, \mathbf{n}_3$ , where  $\mathbf{n}_i \cdot \mathbf{n}_j = \delta_{ij}$

### 2.1 Kinematics

The finite deformation theory employs a multiplicative decomposition of the deformation gradient,  $\mathbf{F}$  into elastic and plastic parts according to

$$\mathbf{F} = \mathbf{F}_e \mathbf{F}_p \quad (1)$$

where the subscripts 'e' and 'p' are used to denote elastic and plastic parts, respectively. This decomposition provides the basis for mapping *continuum* tensors between reference, intermediate, and current configurations consistent with Figure 3. On the other hand, material *substructure* vectors, such as the unit directors  $\mathbf{n}_i$  in Figure 3 do not map according to the continuum motion. Instead we define the orientation of such vectors as

$$\mathbf{n}_i = \mathbf{\Lambda} \mathbf{n}_i^o \quad (2)$$

where  $\mathbf{\Lambda}$  is a proper orthonormal rotation belonging to the special orthogonal group  $\text{SO}(3)$  and, consequently, can be parameterized by three independent variables which we refer to as the rotation vector,  $\boldsymbol{\theta}$ .

The Green-Lagrange strain in the intermediate configuration is obtained by the plastic push forward of the same from the reference configuration,  $\phi_*^p(\mathbf{E})$ , which decomposes additively into elastic and plastic parts in that configuration,

$$\tilde{\mathbf{E}} = \frac{1}{2} (\mathbf{F}_e^T \mathbf{F}_e - \mathbf{I}) + \frac{1}{2} (\mathbf{I} - \mathbf{F}_p^T \mathbf{F}_p^{-1}) \quad (3)$$

The plastic push-forward of the time rate of the plastic part of the deformation gradient, i.e.,  $\phi_*^p(\dot{\mathbf{F}}_p)$ , yields the plastic velocity gradient with respect to the intermediate configuration,

$$\tilde{\mathbf{L}}_p = \dot{\mathbf{F}}_p \mathbf{F}_p^{-1} \quad (4)$$

which can be additively decomposed into symmetric and skew-symmetric parts,  $\tilde{\mathbf{D}}_p = \text{Sym}[\dot{\mathbf{F}}_p \mathbf{F}_p^{-1}]$  and  $\tilde{\mathbf{\Omega}}_p = \text{Skw}[\dot{\mathbf{F}}_p \mathbf{F}_p^{-1}]$ , respectively. Recognizing the contentious source of confusion in the literature in the past regarding these concepts, we employ the convention of Dafalias (2000), in which the plastic continuum spin,  $\tilde{\mathbf{\Omega}}_p$ , is related to the plastic constitutive spin,  $\tilde{\mathbf{W}}_p^j$ , and the substructure spin,  $\hat{\omega}^j$ , for the  $j^{\text{th}}$  substructural element according to

$$\tilde{\mathbf{\Omega}}_p = \tilde{\mathbf{W}}_p^j + \hat{\omega}^j \quad (5)$$

Here we consider only one mechanism associated with substructure directors. Consequently the superscript  $j$  can be dropped from Equation 5, but it is worth mentioning that the theory readily accommodates multiple sets of separately evolving directors because a *spinless* rather than isoclinic intermediate configuration is adopted. The rate of reorientation is obtained using the Lie derivative of Equation 2, i.e.,  $\dot{\mathbf{n}}_i = \widehat{\mathbf{A}}\mathbf{n}_i^o$ , where the time derivative of the rotation tensor is  $\widehat{\mathbf{A}} = \widehat{\boldsymbol{\omega}}\mathbf{A}$  such that the rate of change of unit director vectors is  $\dot{\mathbf{n}}_i = \boldsymbol{\omega} \times \mathbf{n}_i$ . We use the notation  $\widehat{\mathbf{v}}$  to represent the skew tensor whose axial vector is  $\mathbf{v}$ .

Clearly, the plastic constitutive spin,  $\widehat{\mathbf{W}}_p$ , which must be prescribed, defines the relative rate of reorientation of the material substructure,  $\boldsymbol{\omega}$ , with respect to the plastic continuum motion,  $\widehat{\boldsymbol{\Omega}}_p$ . If one selects  $\boldsymbol{\omega} = \mathbf{0}$  then Equation 5 corresponds to an isoclinic intermediate configuration, such as is commonly used in crystal plasticity. On the other hand, we employ  $\widehat{\boldsymbol{\Omega}}_p = \mathbf{0}$  corresponding to a spinless intermediate configuration. This choice offers the advantage that multiple substructure orientations corresponding to, for example, different physical mechanisms can be handled in a straight-forward manner.

## 2.2 Thermodynamics

We assume that the Helmholtz free energy can be expressed in the intermediate configuration as a state function of temperature, elastic strain, orientation of director vectors, and a set of internal state variables introduced to augment the kinematic description of the underlying physical processes, i.e.,  $\psi = \widehat{\psi}(T, \widetilde{\mathbf{E}}_e, \boldsymbol{\theta}, \boldsymbol{\xi}_j)$ . Application of the first and second laws of thermodynamics to reversible (isentropic) and, in turn, isothermal or isoelastic processes yields traditional state relations,

$$\widetilde{\boldsymbol{\Sigma}} = \widetilde{\rho} \frac{\partial \psi}{\partial \widetilde{\mathbf{E}}_e} \quad \widetilde{\mathbf{m}} = \widetilde{\rho} \frac{\partial \psi}{\partial \boldsymbol{\theta}} \quad \widetilde{\boldsymbol{\chi}}_j = \widetilde{\rho} \frac{\partial \psi}{\partial \boldsymbol{\xi}_j} \quad (6)$$

where  $\widetilde{\boldsymbol{\Sigma}}$  is the second Piola-Kirchhoff stress with respect to the intermediate configuration,  $\widetilde{\mathbf{m}}$  is an elastic force conjugate to substructure rotation for cases of elastic anisotropy,  $\widetilde{\boldsymbol{\chi}}_j$  is the thermodynamic driving force conjugate to the internal state variable,  $\boldsymbol{\xi}_j$ , and  $\widetilde{\rho}$  is the mass density per unit volume of the intermediate configuration. Temperature change due to deformation is identified by further manipulation of the first law under arbitrarily dissipative processes,

$$\dot{T} = \frac{1}{\widetilde{\rho}\bar{c}} \left( \widetilde{\boldsymbol{\Sigma}} : \widetilde{\mathbf{D}}_p - \widetilde{\mathbf{m}} \cdot \dot{\boldsymbol{\theta}} - \widetilde{\boldsymbol{\chi}}_j * \dot{\boldsymbol{\xi}}_j \right) - \frac{T}{\bar{c}} \left( \frac{\partial}{\partial T} \frac{\widetilde{\boldsymbol{\Sigma}}}{\widetilde{\rho}} : L_v(\mathbf{E}_e) - \frac{\partial}{\partial T} \frac{\widetilde{\mathbf{m}}}{\widetilde{\rho}} \cdot \dot{\boldsymbol{\theta}} - \frac{\partial}{\partial T} \frac{\widetilde{\boldsymbol{\chi}}_j}{\widetilde{\rho}} * \dot{\boldsymbol{\xi}}_j \right) \quad (7)$$

where  $\bar{c}$  is the specific heat per unit mass and the symbol '\*' is used to reflect the appropriate operator in constructing an inner product for the particular choice of internal state variable. For the model used in this paper we employ isotropic elasticity (thus  $\widetilde{\mathbf{m}} = \mathbf{0}$ ), do not directly represent energy storage, and neglect the thermoelastic coupling such that the temperature change is approximated as

$$\dot{T} \approx \frac{B}{\widetilde{\rho}\bar{c}} \left( \widetilde{\boldsymbol{\Sigma}} : \widetilde{\mathbf{D}}_p \right) \quad (8)$$

where  $B$  is the inelastic heat fraction, taken here as a constant parameter, introduced to reflect the aforementioned effects.

## 2.3 Evolution Kinetics

We consider a threshold (yield) hypersurface in stress space,  $\Upsilon(\widetilde{\boldsymbol{\Sigma}}; \mathbf{n}_i, T, \widetilde{\mathbf{D}}_p, \boldsymbol{\xi}_j) = 0$ . For stress states within the yield surface neither inelastic deformation nor orientation evolution occur, while stress states associated with irreversible processes lie exactly on the yield surface, i.e.,  $\Upsilon\dot{\gamma} = 0$ . The following form for the yield surface is used

$$\Upsilon(\widetilde{\boldsymbol{\Sigma}}; \mathbf{n}_i, T, \widetilde{\mathbf{D}}_p) = \frac{\widetilde{\tau}(\boldsymbol{\Sigma}, \mathbf{n}_i)}{\sigma_y(T, \widetilde{\mathbf{D}}_p, \boldsymbol{\xi}_j)} - 1 \quad (9)$$

where  $\widetilde{\tau}$  is a scalar valued function of the second order tensor,  $\widetilde{\boldsymbol{\Sigma}}$  and the orthogonal set of material directors,  $\mathbf{n}_1, \mathbf{n}_2, \mathbf{n}_3$  and the flow stress,  $\sigma_y$ , is a scalar valued function of the temperature, plastic strain rate, and internal state variables. Employing representation theory, an isotropic scalar valued function of tensoral arguments can

be expressed in terms of invariants forming the integrity basis. One irreducible set of such invariants for three orthogonal vectors and a symmetric second-order tensor is

$$\begin{aligned} I_1 &= \text{Tr} \left[ \mathbf{M}_1 \tilde{\Sigma} \right] & I_2 &= \text{Tr} \left[ \mathbf{M}_2 \tilde{\Sigma} \right] & I_3 &= \text{Tr} \left[ \mathbf{M}_3 \tilde{\Sigma} \right] \\ I_4 &= \text{Tr} \left[ \mathbf{M}_1 \tilde{\Sigma}^2 \right] & I_5 &= \text{Tr} \left[ \mathbf{M}_2 \tilde{\Sigma}^2 \right] & I_6 &= \text{Tr} \left[ \mathbf{M}_3 \tilde{\Sigma}^2 \right] \\ & & I_7 &= \text{Tr} \left[ \tilde{\Sigma}^3 \right] \end{aligned} \quad (10)$$

where the structural tensors  $\mathbf{M}_i = \mathbf{n}_i \otimes \mathbf{n}_i$  have been introduced and are subjected to the constraint  $\mathbf{M}_1 + \mathbf{M}_2 + \mathbf{M}_3 = \mathbf{I}$  to ensure orthonormality. For this work we employ a quadratic function of the invariants, thus

$$\tilde{\tau} = \frac{1}{2}A_1I_1^2 + \frac{1}{2}A_2I_2^2 + \frac{1}{2}A_3I_3^2 + A_4I_4 + A_5I_5 + A_6I_6 + A_8I_1I_2 + A_9I_2I_3 + A_{10}I_1I_3 \quad (11)$$

The evolution of plastic deformation,  $\mathbf{F}_p$ , is defined through the plastic velocity gradient referred to the intermediate configuration according to (4) which is decomposed into symmetric and skew parts as

$$\tilde{\mathbf{L}}_p = \tilde{\mathbf{D}}_p + \tilde{\mathbf{\Omega}}_p \quad (12)$$

The plastic rate of deformation (referred to the intermediate configuration) is assumed normal to a flow pseudopotential  $\Phi \left( \tilde{\Sigma}; \mathbf{n}_i, T, \tilde{\mathbf{D}}_p, \xi_j \right)$  according to

$$\tilde{\mathbf{D}}_p = \dot{\gamma} \mathbf{N}_\Phi \quad (13)$$

where the flow surface normal has been introduced as

$$\mathbf{N}_\Phi = \frac{\frac{\partial \Phi}{\partial \tilde{\Sigma}}}{\left\| \frac{\partial \Phi}{\partial \tilde{\Sigma}} \right\|} \quad (14)$$

In general the flow pseudopotential may be distinct from the yield function, i.e.,  $\Phi \neq \Upsilon$ ; however, in the current work we restrict the model to associated flow such that  $\Phi = \Upsilon$ .

Following Dafalias (1998) and more recently in a finite deformation context Ulz (2011), the *local* plastic constitutive spin is prescribed to be proportional to non-coaxiality between  $\tilde{\Sigma}$  and  $\tilde{\mathbf{D}}_p$ ,

$$\tilde{\mathbf{W}}_p = -\frac{\eta}{\bar{\sigma}} \left( \tilde{\Sigma} \cdot \tilde{\mathbf{D}}_p - \tilde{\mathbf{D}}_p \cdot \tilde{\Sigma} \right) \quad (15)$$

where  $\eta$  is a spin rate coefficient and  $\bar{\sigma}$  is a normalizing stress parameter. Note the negative sign pre-multiplying our  $\eta$  is introduced in order that the corresponding parameter values be positive (as a distinction from the work of Dafalias (1998) and Ulz (2011)). Again, a spinless intermediate configuration is adopted such that  $\tilde{\mathbf{\Omega}}_p = \mathbf{0}$  and, accordingly, the substructure spin is  $\tilde{\omega} = -\tilde{\mathbf{W}}_p$ .

The local substructure spin kinetics are here extended to a nonlocal theory by amplifying or attenuating the local rate of spin based on the extent of misorientation within a nonlocal neighborhood of a material point. The nonlocally enhanced substructure spin is introduced as

$$\tilde{\mathbf{W}}_p^* = \tilde{\mathbf{W}}_p + \|\tilde{\mathbf{W}}_p\| \beta \bar{\theta} \quad (16)$$

where  $\beta$  is a nonlocal spin coefficient and  $\bar{\theta}$  is a nonlocal measure of misorientation between a material point and its surrounding neighborhood. The nonlocal substructure misorientation is defined as the integral of Gaussian weighted difference in orientation angle surrounding the material point at  $\mathbf{x}$ ,

$$\bar{\theta}(\mathbf{x}) = \frac{1}{C_{L\theta}} \int_{\mathbf{y} \in \Omega_\theta(\mathbf{x})} \exp \left[ -\left( \frac{|\mathbf{y} - \mathbf{x}|}{L_\theta} \right)^2 \right] \left( \boldsymbol{\theta}(\mathbf{y}) - \boldsymbol{\theta}(\mathbf{x}) \right) d\Omega_\theta \quad (17)$$

where the normalizing coefficient is computed as

$$C_{L\theta} = \int_{\Omega_\theta} \exp \left[ -\left( \frac{|\mathbf{y} - \mathbf{x}|}{L_\theta} \right)^2 \right] d\Omega_\theta \quad (18)$$

Table 1: Parameters defining shape of yield surface

Description	$A_1$	$A_2$	$A_3$	$A_4$	$A_5$	$A_6$
Isotropic - J2	-1.00	-1.00	-1.00	1.50	1.50	1.50
Tantalum (Bronkhorst et al. 2006)	-1.12	-2.89	-1.12	1.68	2.45	1.68

$\Omega_\theta$  is the nonlocal volume to be integrated over, and  $L_\theta$  is a length scale parameter reflecting the nonlocal interaction distance. While there can be two separate size scales associated with  $\Omega_\theta$  and  $L_\theta$ , respectively, the former reflects a cutoff distance for considering nonlocal interaction, while  $L_\theta$  itself describes the region of emphasis within  $\Omega_\theta$  provided  $\frac{4}{3}\pi L_\theta^3 < \Omega_\theta$ .

### 3 Numerical Simulations

#### 3.1 Constitutive Details

Isotropic and linear hyperelasticity is employed to relate stresses to strains according to  $\tilde{\Sigma} = \mathbb{C} : \tilde{\mathbf{E}}_e$ , where  $\mathbb{C}$  is the standard fourth order elasticity tensor. The top-hat specimens under consideration here were machined from rolled tantalum plate whose initial texture and anisotropic yield surface has been previously characterized (Maudlin et al., 1999, 2003; Bronkhorst et al., 2006). Figure 4 presents pole figures illustrating the initial texture of the stock material and the relationship between the rolled plate material axes and the top-hat specimen axes. Maudlin et al. (1999, 2003) fit a quadratic orthotropic (Hill) yield surface to both experimental and polycrystal simulation results based on the initial texture shown in Figure 4c. Their yield surface was subsequently ‘symmetrized’ about the geometric axis of symmetry for modeling convenience in Bronkhorst et al. (2006). For the top-hat specimen, the initial orientation of the yield surface is assumed to be aligned with the problem axes of symmetry, i.e.,  $\mathbf{n}_1^o = \mathbf{e}_r$  and  $\mathbf{n}_2^o = \mathbf{e}_z$ , where  $\mathbf{e}_r$  and  $\mathbf{e}_z$  are the reference system base vectors aligned in the radial and axial directions, respectively. Substitution of the initial orientation into Equations 10 and 11 and equating to the surface used in Bronkhorst et al. (2006) allows identification of constants  $A_k$  of Equation 11 reported in Table 1.

The flow stress  $\sigma_y(T, \tilde{\mathbf{D}}_p, \xi_j)$  is defined by the mechanical threshold stress model (MTS)

$$\sigma_y = \sigma_a + \frac{\mu(T)}{\mu_0} \left( \hat{\sigma}_I S_I(\dot{\gamma}, T) + \hat{\sigma}_E S_E(\dot{\gamma}, T) \right) \quad (19)$$

where  $\sigma_a$  is the long-range athermal resistance to dislocation glide, for example, due to grain boundaries,  $\hat{\sigma}_I$  reflects the intrinsic lattice resistance to dislocation motion, and  $\hat{\sigma}_E$  reflects evolving barriers to dislocation motion such as interactions with dislocation forests. The thermal activation functions,  $S_I$  and  $S_E$ , reflect the increased probability of a dislocation overcoming the threshold resistance at increasing temperature and decreasing strain rate consistent with thermally activated processes as described by Kocks et al. (1975). For details of the MTS flow stress model cf. Follansbee and Kocks (1988); Chen and Gray (1996); Maudlin et al. (1999); Bronkhorst et al. (2006). Figure 5 compares uniaxial stress-strain data from experiments to the MTS model fit for tantalum. The experimental data is from Chen and Gray (1996) and all constitutive parameters and form of evolution equation for  $\hat{\sigma}_E$  are the same as those given in Maudlin et al. (1999); Bronkhorst et al. (2006). From this figure the MTS model does a reasonable job representing the temperature and rate-dependence of the flow stress for these uniaxial (moreover monotonic and proportional) strain histories.

#### 3.2 Implementation

The model was implemented as a total-Lagrangian stabilized selectively-reduced-integration axisymmetric solid element within the user defined subroutine VUEL in Abaqus. At each integration point within an element, the update of the constitutive state employs semi-implicit integration via an exponential map of the plastic increment to evolve the plastic part of the deformation gradient. The algorithm is implicit in the plastic strain rate,  $\dot{\gamma}$ , but explicit in the flow direction, temperature, mechanical threshold stress, and substructure spin update. Given the small time steps required for global stability, this semi-implicit scheme is presumed sufficient. The calculation of stresses employs a hyperelastic update in the intermediate configuration which is pulled back to the reference configuration by the plastic part of the deformation gradient.

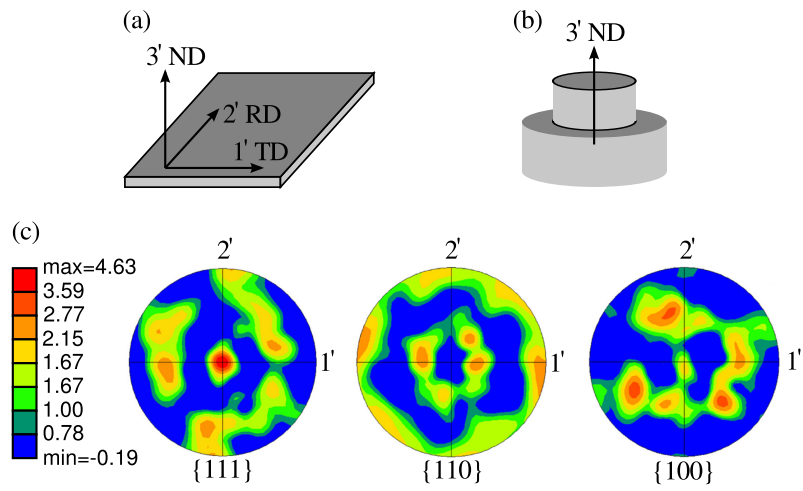


Figure 4: Initial orthotropic texture and orientation. (a) rolled plate stock and material axes (b) top-hat specimen and specimen axes (c) pole figures indicating initial texture viewed along normal direction (ND)

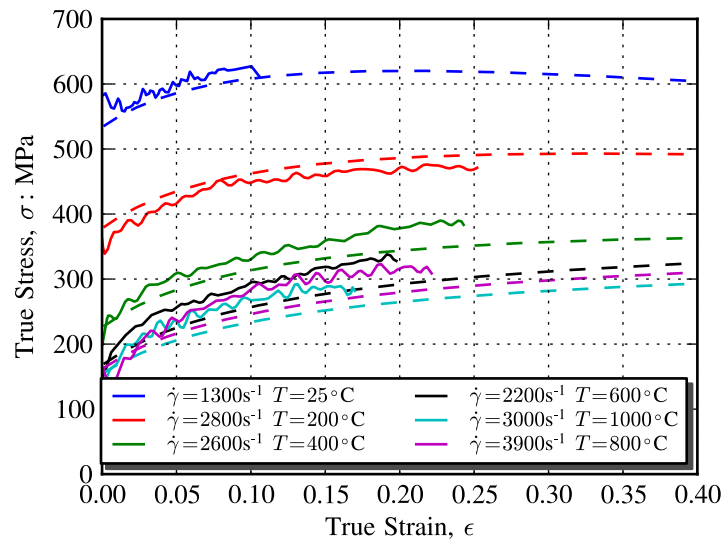


Figure 5: Stress vs. strain behavior for tantalum solid indicates experimental data and dashed represents the MTS model fit

Table 2: Dimensions (mm) used for top-hat simulations corresponding to diagram in Figure 1

$r_1$	$r_2$	$r_3$	$h_1$	$h_2$	$h_3$
2.09	2.28	4.30	2.60	3.47	5.11

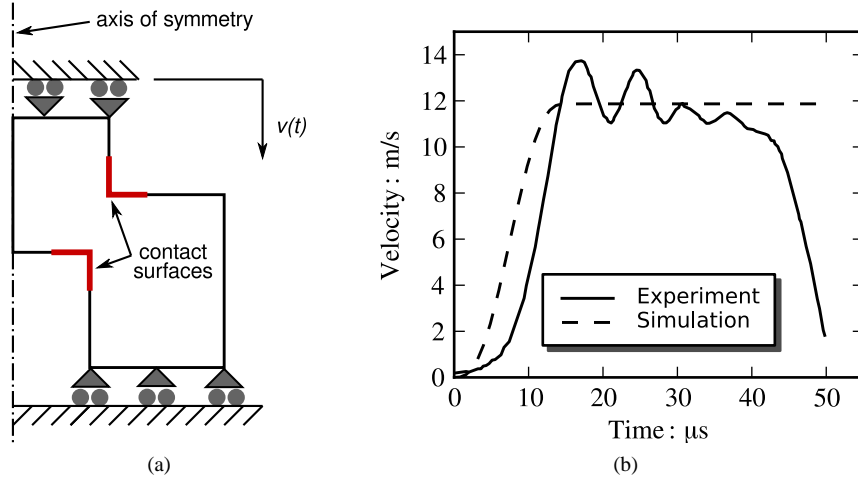


Figure 6: Finite element model details. (a) geometry and boundary conditions (b) velocity time history applied to upper platen

The finite element model of the top-hat utilizes the axisymmetry of the specimen geometry as depicted in Figure 6a. The physical dimensions of the top-hat specimen are provided in Table 2. Boundary conditions are specified along the bottom edge of the finite element model to restrain only vertical components of motion, i.e., nodes along this edge are unrestrained in the radial direction. The velocity time history shown in Figure 6b is prescribed for the vertical motion of nodes along the top surface of the model. Only the specimen is modeled; details of the split Hopkinson pressure bar apparatus are not modeled and, consequently, the reflection of inertial waves in the actual system cannot be accurately predicted. Accordingly, a smoothed velocity profile was used to reduce inertial ringing in the model otherwise caused by reflection of momentum off the perfectly rigid boundaries. Contact surfaces are specified as indicated in Figure 6a to prevent material inter-penetration under severe deformation of the sharp corner regions. Constitutive parameters for the MTS flow stress model are taken directly from Maudlin et al. (1999); Bronkhorst et al. (2006). Simulations were run to approximately  $35\mu s$  in simulation time employing a fixed time step size of  $\Delta t = 2.0e - 10s$  under varying parameter values as discussed in the next section. A contour plot of the effective plastic strain,  $\bar{\epsilon}_p$ , from a representative case is shown in Figure 7. The deformation is concentrated in a relatively sharp band within the shear zone. For that reason, subsequent contour plots only show the shear zone as indicated by the red inset region in Figure 7. Additionally, the white arrow in this plot approximately indicates a reference axis across which contour results are sampled to compare spatial distributions of field variables such as plastic strain across the shear band. For example, consider the plot of effective plastic strain versus distance along this reference axis shown in Figure 8a. Finally, we also compare results for the normal stress, i.e., the total applied force normalized by initial top surface area, versus displacement of the top platen toward the bottom platen as shown in Figure 8b.

#### 4 Results and Discussion

Classic finite element discretization of local continuum theories is well known to exhibit artificial mesh dependence for problems that exhibit strong localization. Traditionally, this behavior is demonstrated by comparing results for increasingly refined spatial meshes. To assess this tendency simulations were conducted using meshes with five different characteristic element sizes. Figure 9 shows the finite element grid within the shear zone region for each element size,  $h$ . The mesh transitioned to a coarser size of approximately  $h = 150\mu m$  outside the shear zone region for all cases. These simulations were conducted using a spin rate coefficient of  $\eta = 100$  combined with a purely local constitutive plastic spin, i.e.,  $\beta = 0$ .

Nominal stress versus platen displacement results shown in Figure 10a exhibit convergence of simulation results toward the experimental values. While not quantified here, such convergence indicates that the global response is

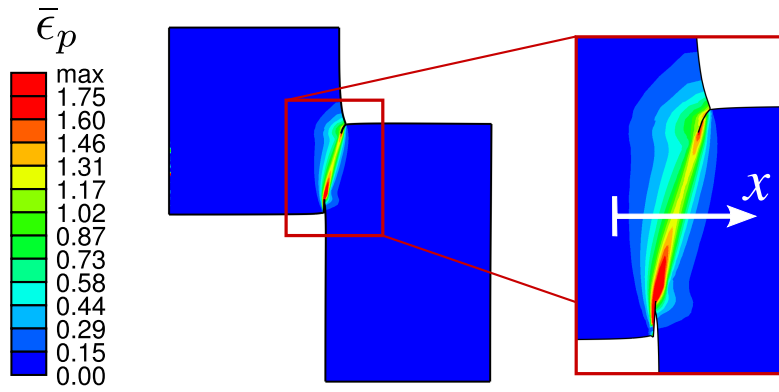


Figure 7: Contour plot of plastic strain,  $\bar{\epsilon}_p$ . Magnified inset region approximately corresponds to shear zone and is used for all subsequent contour plots. White arrow in inset region indicates position axis used for plots such as Figure 8b

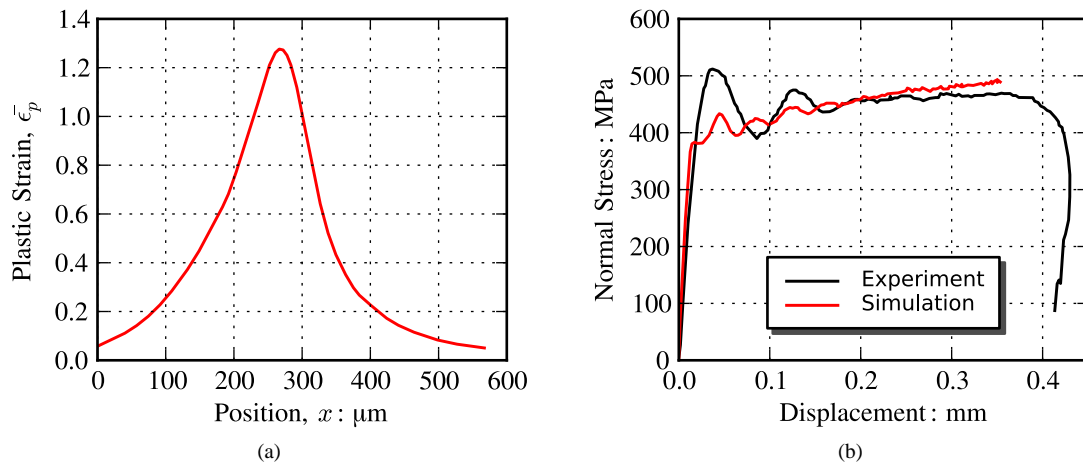


Figure 8: Example results. (a) Distribution of equivalent plastic strain across shear zone. (b) Comparison between experiment and simulation of normal stress versus top platen displacement

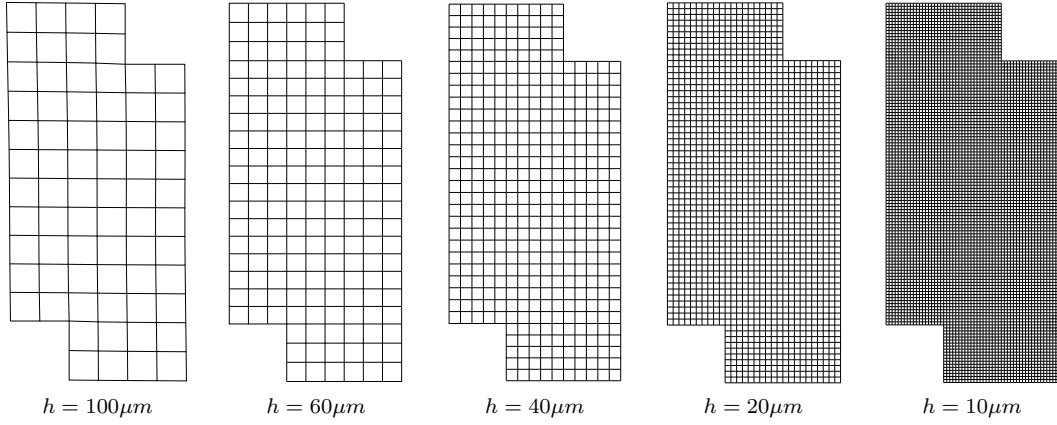


Figure 9: Finite element meshes used in mesh refinement study. Only the shear zone region is shown.

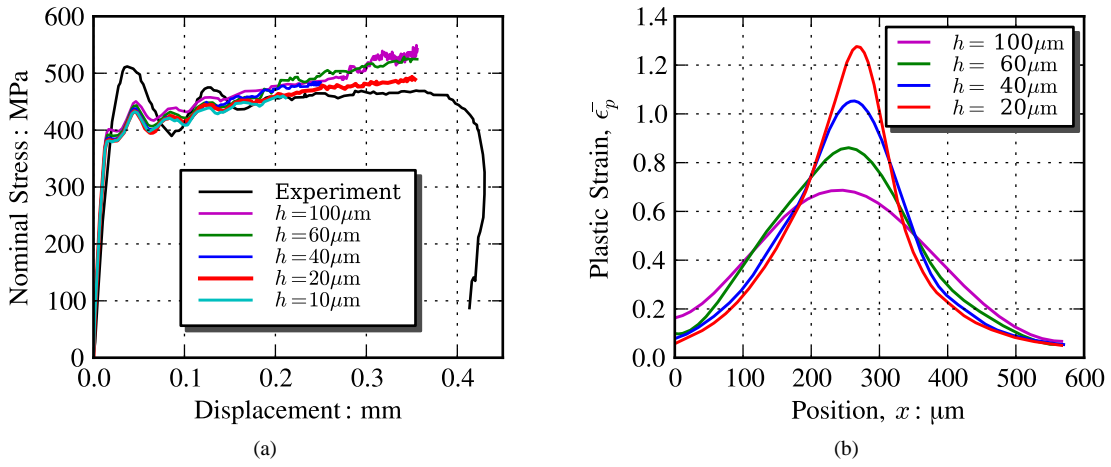


Figure 10: Results for varying mesh element size,  $h$ . (a) Normal stress versus platen displacement (b) Distribution of equivalent plastic strain,  $PEEQ$ , across shear zone.

not artificially dependent on the mesh. On the other hand, Figure 10b indicates that the distribution of effective plastic strain,  $\bar{\epsilon}_p$ , across the shear zone is exhibiting an artificial dependence on the finite element mesh. Essentially, there is some degree of localization occurring within the shear zone, but it is subdued such that the global character of the problem is unchanged. Subsequent simulations employ the mesh whose characteristic element size is  $h = 20\mu m$ .

To assess the influence of local substructure spin rate on these results, simulations using local evolution kinetics, i.e.,  $\beta = 0$  and varying values of the local spin coefficient  $\eta$  were conducted. Nominal-stress versus platen-displacement results shown in Figure 11a indicate that increases in local spin coefficient are associated with decreased global hardening. Figure 11b compares the effective plastic strain across the shear zone for differing spin rate coefficients at the final deformed state,  $t = 37.5\mu s$ . Increasing values of spin rate coefficient from 0 to 10 result in a sharper more pronounced band of effective plastic strain; however, the plastic strain distribution for a spin rate coefficient of 100 is relatively subdued by contrast to the  $\eta = 10$  case.

The substructure orientation vector field,  $\mathbf{n}_2$ , at the final deformed state is represented by white arrows superposed over contour plots of effective plastic strain in Figure 12 for each value of spin rate coefficient simulated. In all cases there is a locally enhanced region of plastic deformation at the sharp reentrant corners of the specimen. The reorientation of substructure within the band of plastic deformation, and likewise, the extent that enhanced plastic deformation propagates from each corner toward the center, both increase with spin rate coefficient to a value of  $\eta = 10$ . However, consistent with Figure 11, the plastic strain in the center of the band has been subdued relative to that in the  $\eta = 10$  case. For cases  $\eta = 10$  and  $\eta = 100$  substructure reorientation is significant in a region extending beyond the zone of intense plastic deformation. Profiles of the (clockwise) rotation angle of material substructure vector  $\mathbf{n}_2$  across the shear zone are plotted in Figure 13a and the evolution time history corresponding to the center of these profiles are shown in Figure 13b. From  $x = 100$  to  $500$  there is a region of clockwise

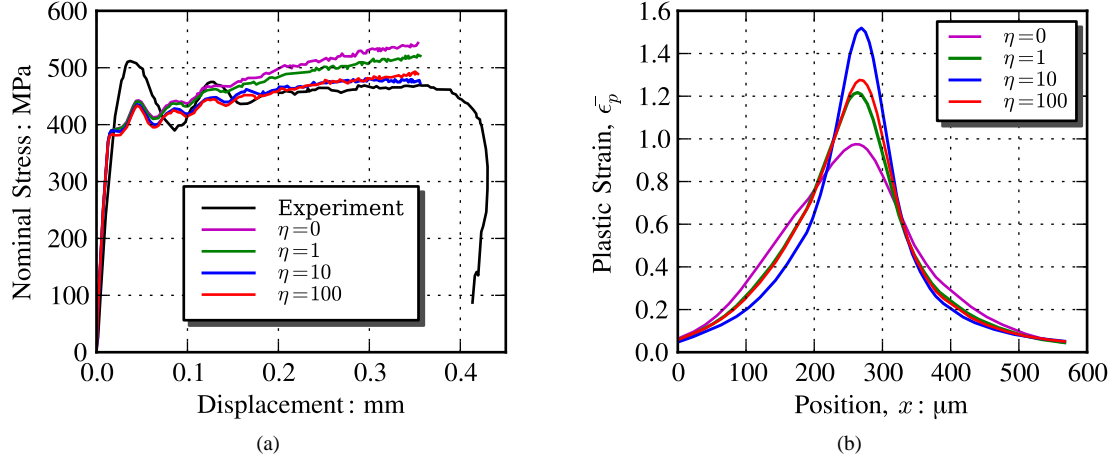


Figure 11: Results for various values of spin coefficient,  $\eta$ . (a) Normal stress versus platen displacement (b) Distribution of equivalent plastic strain,  $\bar{\epsilon}_p$ , across shear zone.

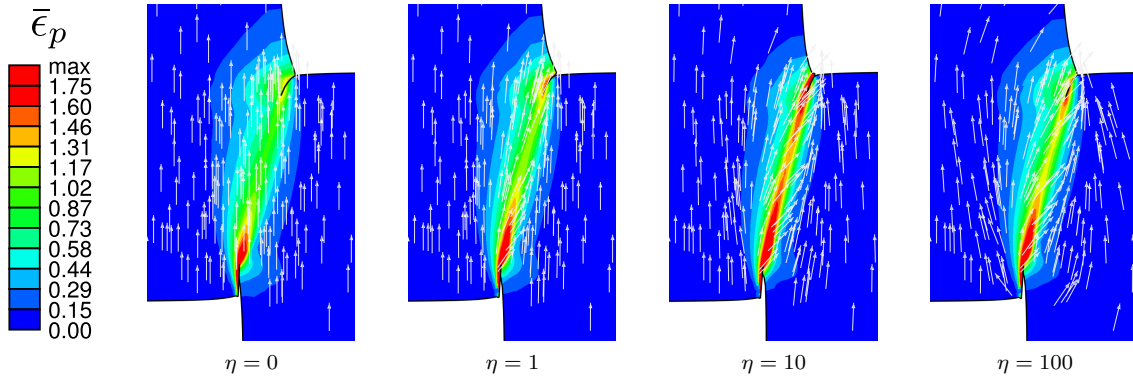


Figure 12: Contour plots of effective plastic strain,  $\bar{\epsilon}_p$ , at the final deformed state ( $t = 37.5 \mu\text{s}$ ) for various values of spin rate coefficient  $\eta$ . White arrows indicate the orientation of substructure director vector,  $\mathbf{n}_2$ .

reorientation for all cases of nonzero spin rate. For  $\eta = 1$ , this reorientation and its gradient tend toward zero outside the shear zone. On the other hand, the cases of  $\eta = 10$  and  $100$  result in a counterclockwise reorientation outside this region. The temporal evolution of substructure orientation shows a monotonically increasing angle with monotonically increasing spin rate for  $\eta = 1$ . For  $\eta = 10$  the reorientation increases monotonically as well; however, the early spin rate is much higher than for  $\eta = 1$  and decreases subsequently. The case of  $\eta = 100$  begins with an even larger initial spin rate as plastic deformation initiates, but appears to overshoot some preferred orientation and exhibits a non-monotonic ‘correction’ that subsequently becomes similar to the  $\eta = 10$  curve. None of these cases saturate to a final orientation such as observed in experiments and simulations with a fixed orientation of loading (Dafalias, 1998, 2000; Bunge and Nielsen, 1997; Ulz, 2011). The continued evolution is characteristic of non-proportional loading, i.e., the orientation of stress continues to evolve during the deformation process.

The substructure reorients such that the principal axes of the orthotropic yield surface align in an orientation more favorable for continued yielding with respect to the current stress state. Increasing the spin rate coefficient enables such reorientation to occur more immediately, while reducing the spin rate coefficient resists such reorientation. Clearly, the reorientation of substructure is an additional constitutive softening mechanism independent of softening due to damage or dissipative heat generation. This contributor to softening behavior is often overlooked in application to formation of shear band or necking instabilities in high deformation-rate applications.

The spatial misorientation exhibited in Figure 12 as characterized by strong fluctuations in orientation angle exposes a conceptual disconnect between local theories of substructure evolution and the observations made in the introduction of this paper supporting a nonlocal theory for substructure reorientation kinetics. Conceptually, the orientation of the yield surface at any macroscopic material point reflects the collective orientation of active slip systems at a finer (crystal) scale within some neighborhood of influence. Gradients of substructure orientation then, in effect, are reflective of underlying lattice curvature combined with evolution of intragranular misorienta-

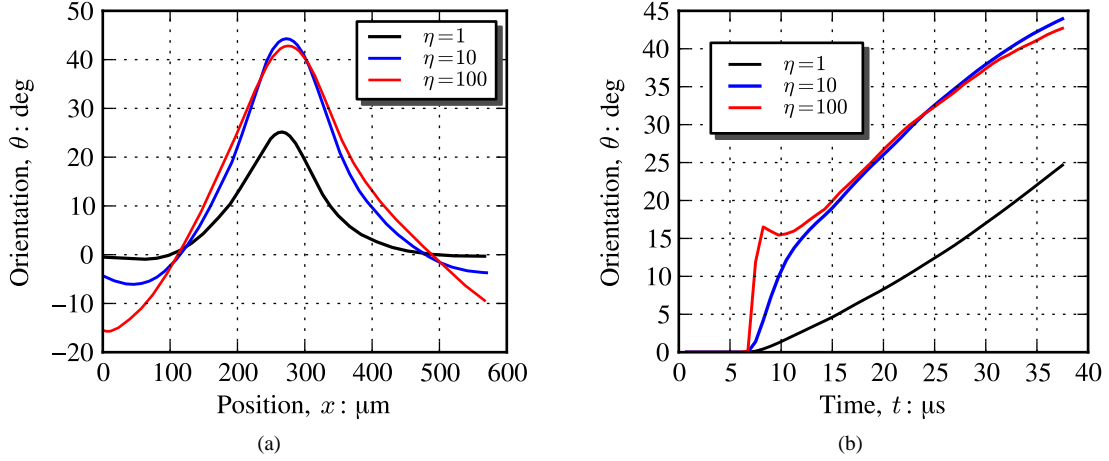


Figure 13: Orientation evolution for various values of spin coefficient,  $\eta$ . (a) Distribution of orientation,  $\theta$ , across shear zone at  $t = 37.5\mu\text{s}$ . (b) Orientation time history at location in center of shear zone

tion. Both of these mechanisms have energetic consequence, thus one expects some resistance to sharp gradients in spatial misorientation at the coarse scale. In other words, the material substructure associated with neighboring continuum material points cannot spin independent of each other. This reasoning combined with previous observations motivated the nonlocal form of constitutive plastic spin of Equation 16. To demonstrate the influence of nonlocal substructure evolution, results for a simulation with  $\beta = 8$  and  $L_\theta = 100\mu\text{m}$  are compared to corresponding local simulations, i.e.  $L_\theta = 0$  and  $\beta = 0$ , for a spin coefficient of  $\eta = 10$ .

In particular, the effective plastic strain,  $\bar{\epsilon}_p$ , and clockwise rotation angle,  $\theta$ , are plotted versus position for the local and nonlocal cases in Figure 14 (a) and (b), respectively. The band of plastic deformation is broader with a lower peak for the nonlocal case relative to the local case. Likewise, the distribution of orientation angle is flattened considerably for the nonlocal case. While the maximum gradient of rotation (curvature) appears consistent between the two cases the second gradient of rotation, corresponding to a curvature gradient, is significantly reduced.

The suppression of curvature gradients, while leaving the maximum curvature essentially unaltered can be explained by expanding the misorientation in the vicinity of a material point into a Taylor series,

$$\Delta\theta(\mathbf{x}) = \theta(\mathbf{y}) - \theta(\mathbf{x}) = \theta \overleftarrow{\nabla}|_{\mathbf{x}} \cdot (\mathbf{y} - \mathbf{x}) + \theta \overleftarrow{\nabla} \overleftarrow{\nabla}|_{\mathbf{x}} : (\mathbf{y} - \mathbf{x}) \otimes (\mathbf{y} - \mathbf{x}) + \dots \quad (20)$$

The leading term on the right hand side (RHS) of Equation 20 is the linear variation of  $\theta$  associated with its first gradient or curvature evaluated at the material point located at  $\mathbf{x}$ . Within Equation 17, the weighted integral of the first term from the RHS of Equation 20 over  $\Omega_\theta$  is zero because the variation is linear across the volume and the weighting is symmetric. Consequently, the curvature is not penalized by the nonlocal spin kinetics of Equation 16. The same argument does not apply to the next term in the Taylor series reflecting the gradient of curvature, because  $\int (\mathbf{y} - \mathbf{x}) \otimes (\mathbf{y} - \mathbf{x})$  is not zero over the domain,  $\Omega_\theta$ .

Comparison of the effective plastic strain contours and substructure orientation shown in Figure 15 illustrates that the transition in orientation across the band appears more coherent for the nonlocal case than for the local case. For the nonlocal case, within the banded region, the preferred direction of the yield surface reorients essentially parallel to a (virtual) line connecting the sharp specimen corners within the shear zone. Overall, the constraints presented by nonlocal evolution of substructure orientation affects the plastic deformation field by reducing the propensity for flow.

## 5 Summary and Concluding Remarks

In this work, we have implemented local and nonlocal kinetics for substructure orientation evolution into a finite-deformation hyperelastic-plastic constitutive framework. The constitutive implementation employs an isotropic hardening based on an evolving mechanical threshold stress suitable for application to high strain-rates. The yield surface is of Hill type, quadratic in deviatoric stress space and possessing orthotropic symmetry. Substructure evolution reflects the reorientation of this surface within stress space of the intermediate configuration, while the

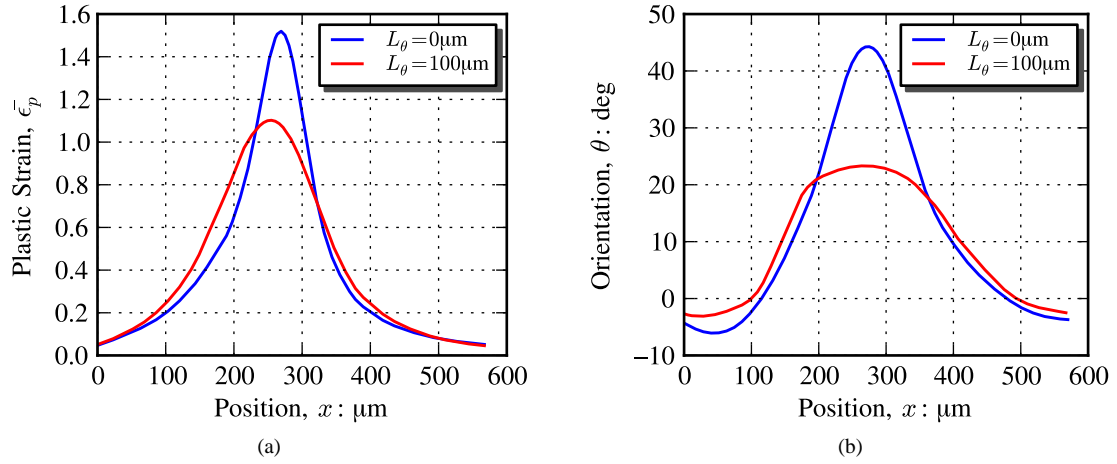


Figure 14: Distribution of field variables across shear zone at  $t = 35 \mu s$  for  $\beta = 8$  and varying length scale parameter,  $L_\theta$ . (a) Effective plastic strain,  $\bar{\epsilon}_p$  (b) Orientation,  $\theta$

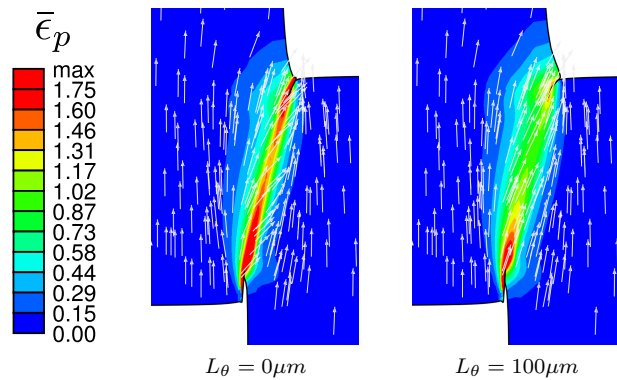


Figure 15: Contour plots of effective plastic strain,  $\bar{\epsilon}_p$ , at the final deformed state ( $t = 37.5 \mu s$ ) for various values of nonlocal length scale parameter  $L_\theta$ . White arrows indicate the orientation of substructure director vector,  $\mathbf{n}_2$ .

isotropic hardening provides for an affine enlargement of the surface. The theory can be extended to accommodate more general evolution of the shape of the yield surface.

Application of the local and nonlocal substructure reorientation kinetics to the problem of high-rate compression of top-hat specimen provides several insights regarding the role of such reorientation on the formation of shear bands and potential for fragment formation. Firstly, when anisotropy of the yield surface is cast in the intermediate configuration, restraint of substructure reorientation resists the formation of shear bands. Conversely, increased substructure spin enables the substructure to align in a preferred orientation that most readily accommodates plastic deformation. However, increasingly larger values of the spin coefficient lead to misorientation fields that are perhaps aphysical. A nonlocal plastic constitutive spin was prescribed by penalizing the local substructure evolution rate based on the weighted misorientation within a neighborhood of a material point resulting in increased spatial coherence of substructure orientation accompanied by restrained plastic deformation.

The results presented demonstrate that substructure evolution is an important contributor to constitutive softening beyond such degradation attributed to damage or thermally decreased flow stress caused by dissipative heat generation. This aspect of constitutive softening takes on an important role in enhancing or attenuating the formation of macroscale shear bands; thus, the kinetics of substructure reorientation are an important aspect of macroscale constitutive modeling in cases of localization and potential ductile fracture or fragmentation. Furthermore, there are both physical and numerical grounds justifying nonlocal evolution kinetics for substructure orientation. Such nonlocal kinetics require explicit specification of a length scale parameter, the value of which directly relates to the size of neighborhood that influences the response at a material point. It is conceivable that such a parameter will depend upon both the long range character of the boundary value problem and the current state of the material, although identification of such relationships is beyond the scope of the present work.

While the extension of classical local plastic constitutive spin kinetics to reflect nonlocal interactions was introduced in a relatively ad hoc manner, the results presented here motivate and provide some context for a finite-deformation micropolar theory of substructure reorientation. Ideally, the development of such a theory should be tightly coupled with ongoing experiments studying texture evolution and finer scale simulations to relate polycrystal texture evolution to generally nonassociative shape and orientation of macroscale yield surfaces.

### Acknowledgements

The authors would like to acknowledge Dr. H. Mourad for providing guidance on the implementation of contact with user-defined elements, discussions with Dr. J. Mayeur on nonlocal reorientation kinetics, and Dr. F. Ad-dessio for discussions and reviewing the manuscript. The work was conducted, in part, under the DOE Advanced Simulation and Computing program.

### References

- Bronkhorst, C. A.; Cerreta, E. K.; Xue, Q.; Maudlin, P. J.; Mason, T. A.; Gray, G. T.: An experimental and numerical study of the localization behavior of tantalum and stainless steel. *Int. J. Plasticity*, 22, 7, (2006), 1304–1335.
- Bronkhorst, C. A.; Hansen, B. L.; Cerreta, E. K.; Bingert, J. F.: Modeling the microstructural evolution of metallic polycrystalline materials under localization conditions. *J. Mech. Phys. Solids*, 55, 11, (2007), 2351–2383.
- Bunge, H. J.; Nielsen, I.: Experimental determination of plastic spin in polycrystalline materials. *Int. J. Plasticity*, 13, 5, (1997), 435–446.
- Chen, S. R.; Gray, G.: Constitutive behavior of tantalum and tantalum-tungsten alloys. *Metallurgical And Materials Transactions A (Physical Metallurgy And Materials Science)*, 27A, 10.
- Dafalias, Y. F.: Plastic spin: Necessity or redundancy? *Int. J. Plasticity*, 14, 9, (1998), 909–931.
- Dafalias, Y. F.: Orientational evolution of plastic orthotropy in sheet metals. *J. Mech. Phys. Solids*, 48, 11, (2000), 2231–2255.
- Follansbee, P. S.; Kocks, U. F.: A constitutive description of the deformation of copper based on the use of the mechanical threshold stress as an internal state variable. *Acta Metallurgica*, 36, 1, (1988), 81–93.
- Kocks, U. F.; Argon, A. S.; Ashby, M. F.: Thermodynamics and kinetics of slip. *Progress in Materials Science*, 19, (1975), 1–281.

- Kuroda, M.: Roles of plastic spin in shear banding. *Int. J. Plasticity*, 12, 5, (1996), 671–693.
- Lee, H.; Im, S. Y.; Atluri, S. N.: Strain localization in an orthotropic material with plastic spin. *Int. J. Plasticity*, 11, 4, (1995), 423–450.
- Maudlin, P. J.; Bingert, J. F.; Gray, G.: Low-symmetry plastic deformation in BCC tantalum: experimental observations, modeling and simulations. *Int. J. Plasticity*, 19, 4, (2003), 483–515.
- Maudlin, P. J.; Bingert, J. F.; House, J. W.; Chen, S. R.: On the modeling of the Taylor cylinder impact test for orthotropic textured materials: experiments and simulations. *Int. J. Plasticity*, 15, 2, (1999), 139–166.
- Nemat-Nasser, S.; Li, Y. F.; Isaacs, J. B.: Experimental/computational evaluation of flow stress at high strain rates with application to adiabatic shear banding. *Mechanics of Materials*, 17, 2-3.
- Tvergaard, V.; van der Giessen, E.: Effect of plastic spin on localization predictions for a porous ductile material. *J. Mech. Phys. Solids*, 39, 6, (1991), 763–781.
- Ulz, M.: A finite isoclinic elasto-plasticity model with orthotropic yield function and notion of plastic spin. *Computer Methods in Appl. Mechanics Engineering*, 200, 21-22, (2011), 1822–1832.
- Zbib, H. M.: On the mechanics of large inelastic deformations - kinematics and constitutive modeling. *Acta Mechanica*, 96, 1-4, (1993), 119–138.
- Zbib, H. M.; Aifantis, E. C.: On the concept of relative and plastic spins and its implications to large deformation theories .1. hypoelasticity and vertex-type plasticity. *Acta Mechanica*, 75, 1-4, (1988a), 15–33.
- Zbib, H. M.; Aifantis, E. C.: On the concept of relative and plastic spins and its implications to large deformation theories .2. anisotropic hardening plasticity. *Acta Mechanica*, 75, 1-4, (1988b), 35–56.

---

*Address:* Dr. Darby J. Luscher and Dr. Curt A. Bronkhorst. Fluid Dynamics and Solid Mechanics Group, Theoretical Division, Los Alamos National Laboratory, Los Alamos, NM 87544.  
Dr. Prof. David L. McDowell. George W. Woodruff School of Mechanical Engineering, School of Material Science and Engineering, Georgia Institute of Technology, Atlanta, GA 30332  
email: djl@lanl.gov; cabronk@lanl.gov; david.mcdowell@me.gatech.edu